Published in final edited form as:

Neuroimage. 2016 February 15; 127: 456–471. doi:10.1016/j.neuroimage.2015.10.034.

Improved Determination of the Myelin Water Fraction in Human Brain using Magnetic Resonance Imaging through Bayesian Analysis of mcDESPOT

Mustapha Bouhrara and **Richard G. Spencer**

Magnetic Resonance Imaging and Spectroscopy Section, Laboratory of Clinical Investigation, National Institute on Aging, National Institutes of Health, Baltimore, MD 21224, USA

Abstract

Myelin water fraction (MWF) mapping with magnetic resonance imaging has led to the ability to directly observe myelination and demyelination in both the developing brain and in disease. Multicomponent driven equilibrium single pulse observation of T_1 and T_2 (mcDESPOT) has been proposed as a rapid approach for multicomponent relaxometry and has been applied to map MWF in human brain. However, even for the simplest two-pool signal model consisting of MWF and non-myelin-associated water, the dimensionality of the parameter space for obtaining MWF estimates remains high. This renders parameter estimation difficult, especially at low-to-moderate signal-to-noise ratios (SNR), due to the presence of local minima and the flatness of the fit residual energy surface used for parameter determination using conventional nonlinear least squares (NLLS)-based algorithms. In this study, we introduce three Bayesian approaches for analysis of the mcDESPOT signal model to determine MWF. Given the high dimensional nature of mcDESPOT signal model, and, thereby, the high dimensional marginalizations over nuisance parameters needed to derive the posterior probability distribution of MWF parameter, the introduced Bayesian analyses use different approaches to reduce the dimensionality of the parameter space. The first approach uses normalization by average signal amplitude, and assumes that noise can be accurately estimated from signal-free regions of the image. The second approach likewise uses average amplitude normalization, but incorporates a full treatment of noise as an unknown variable through marginalization. The third approach does not use amplitude normalization and incorporates marginalization over both noise and signal amplitude. Through extensive Monte Carlo numerical simulations and analysis of *in-vivo* human brain datasets exhibiting a range of SNR and spatial resolution, we demonstrated the markedly improved accuracy and precision in the estimation of MWF using these Bayesian methods as compared to the stochastic region contraction (SRC) implementation of NLLS.

Address correspondence to: Mustapha Bouhrara, Ph.D., bouhraram@mail.nih.gov, or Richard G. Spencer, M.D., Ph.D., NIH/National Institute on Aging, Intramural Research Program, BRC 04B-116, 251 Bayview Boulevard, Baltimore, MD 21224, USA., Tel: 410-558-8226 spencer@helix.nih.gov.

Keywords

mcDESPOT; Myelin water fraction; Bayesian analysis; Stochastic region contraction algorithm; Nonlinear least squares; Brain

1. INTRODUCTION

Myelination changes are an important feature of brain development (1) and of the pathophysiology of a number of central nervous system diseases including multiple sclerosis (2-3), phenylketonuria (4-5), schizophrenia (6), epilepsy (7) and psychotic disorders (8), and has been recently associated with Alzheimer's disease (9). Magnetic resonance imaging (MRI) methods for assessing myelination have been developed around the concept of the MRI-visible myelin water fraction (MWF) (10), conventionally measured through multicomponent T_2 analysis of transverse signal decay data acquired using multiple spin echo-based sequences, such as the classic Carr-Purcell-Meiboom-Gill (11-16) or the gradient- and spin-echo (17) sequences.

Multicomponent driven equilibrium single pulse observation of T_1 and T_2 (mcDESPOT) has been proposed as an alternative approach to multicomponent relaxometry with greatly reduced acquisition time and making use of conventional MR acquisition sequences (18), namely, spoiled gradient recalled echo (SPGR) and fully balanced steady state free precession (bSSFP), with, for both sequences, imaging data acquired over multiple flip angles (FA) with a very short repetition time (TR). mcDESPOT has been applied to map MWF in human brain (19-23) with data acquisition sufficiently rapid to permit whole brain coverage. However, Bouhrara *et al.* (24) showed that, even for a simple two-pool model, quantitative parameter estimation from mcDESPOT is problematic, especially at low-to-moderate SNR. This parameter instability was found to persist in spite of the use of stochastic region contraction (SRC) in combination with nonlinear least squares (SRC-NLLS) algorithm, which has been proposed as an effective procedure for extracting parameter values from mcDESPOT data (25-26). It has been found (24) that given the flatness of NLLS parameter fit energy surfaces, SRC-NLLS remains highly sensitive to local minima and requires, therefore, high SNR data for reliable estimation of MWF. This limits the utility of mcDESPOT for the high resolution whole brain mapping studies required to detect spatial changes in MWF and to reduce partial volume effects.

Several previous studies have established the potential benefits of the Bayesian probability approach to parameter estimation (27-31). Indeed, unlike NLLS-based algorithms, Bayesian analysis does not require initial estimates, so that derivation of the posterior probability distribution function (PDF) for a given parameter is less sensitive to the local minimum structure of the global fit function. In addition, Bayesian analysis permits the incorporation of prior probability distributions. In favorable cases, the product of a prior and the likelihood function can be integrated analytically, serving to decrease the dimensionality of the integrations required to derive the posterior PDF of a given parameter (30).

In this study, we investigated the accuracy and precision of MWF determination from a two-component mcDESPOT model using three Bayesian-based methods. As is conventional, the

MWF was defined as the amplitude of the component with the smaller value for T_2, reflecting a motionally-restricted water pool. We compared these results with those derived using SRC-NLLS. We first review the theory of the two-pool mcDESPOT signal model. We then describe in detail our Bayesian approaches for MWF mapping using mcDESPOT. Next, we present extensive Monte Carlo (MC) simulations that give the relative bias and dispersion in the estimation of MWF for several underlying input parameters as a function of SNR, using the SRC-NLLS- and the Bayesian-based approaches. Finally, we present MWF maps obtained from human brain datasets that exhibit a range of SNR and spatial resolution.

2. THEORY

2.1. The Two-pool mcDESPOT Signal Model

mcDESPOT is based on the use of SPGR and bSSFP datasets, each acquired over a range of FAs, with very short TR (18, 32). Neglecting exchange between components, the two-component SPGR signal is conventionally given by (33)

$$M_{SPGR}^{k}=M_{SPGR}^{0}\quad \sin\left(B_1\alpha_k\right)\left(f_s\frac{1-E_{1,s}}{1-E_{1,s}\cos\left(B_1\alpha_k\right)}+\left(1-f_s\right)\frac{1-E_{1,l}}{1-E_{1,l}\cos\left(B_1\alpha_k\right)}\right) \quad [1]$$

where the dimensionless quantity B_1 denotes an RF transmit scaling factor, s and l respectively denote the short- and long- T_2 components, f_s is the fraction of the short T_2 component, M_0^{SPGR} represents the signal amplitude at echo time TE = 0 and incorporates proton density and machine factors, and α_k is the k^{th} excitation FA out of a total of K FAs. We also define $E_{1,j} = exp(-\mathrm{TR}_{SPGR}/T_{1,j})$, where $T_{1,j}$ is the spin-lattice relaxation time of the j^{th} component.

Similarly, the two-component bSSFP signal in the absence of exchange between components is conventionally given by (34)

$$M_n^{bSSFP}\left|M_{bSSFP}^{0}\left(f_s\left(M_{a,s}^{n}+iM_{b,s}^{n}\right)+\left(1-f_s\right)\left(M_{a,l}^{n}+iM_{b,l}^{n}\right)\right)\right|, \quad [2]$$

where

$$M_{a,j}^{n}=\frac{E_{2,j}\left(1-E_{1,j}\right)\quad \sin\left(B_1\beta_n\right)\quad \sin\varphi}{\left(1-E_{1,j}\cos\left(B_1\beta_n\right)\right)\left(1-E_{2,j}\cos\varphi\right)-E_{2,j}\left(E_{1,j}-\cos\left(B_1\beta_n\right)\right)\left(E_{2,j}-\cos\varphi\right)}$$

and

$$M_{a,j}^{n}=\frac{E_{2,j}\left(1-E_{1,j}\right)\left(\cos\varphi-E_{2,j}\right)\quad \sin\left(B_1\beta_n\right)}{\left(1-E_{1,j}\cos\left(B_1\beta_n\right)\right)\left(1-E_{2,j}\cos\varphi\right)-E_{2,j}\left(E_{1,j}-\cos\left(B_1\beta_n\right)\right)\left(E_{2,j}-\cos\varphi\right)}.$$

Here, j indicates the short (s) or long (l) T_2 species, M_{bSSFP}^{0} represents the bSSFP signal amplitude at echo time TE = 0 and incorporates proton density and machine factors, β_n is the n^{th} excitation FA out of a total of N FAs, and $\phi = 2\pi\cdot\Delta\omega\cdot \mathrm{TR}_{bSSFP} + \vartheta$, with $\Delta\omega$ the off-resonance frequency of proton pools with the assumption that both proton pools exhibit the

same chemical shift, and ϑ the phase increment of the applied radio-frequency (RF) pulse. $E_{1,j} = exp(-TR_{bSSFP}/T_{1,j})$ and $E_{2,j} = exp(-TR_{bSSFP}/T_{2,j})$, where $T_{2,j}$ is the spin-spin relaxation time of the j^{th} component.

In our simulation analyses, the FAs were assumed to be well-calibrated (*i.e.* $B_1 = 1$) and the two proton pools were assumed to be on-resonance (*i.e.* $\Delta\omega = 0$ Hz), while in the experimental analyses, B_1 and $\Delta\omega$ were calculated using the saturated double angle method (S-DAM) (35) and the DESPOT$_2$-FM method (36), respectively, and used as known parameters for the calculation of the f_s maps, reflecting MWF. Further, in all cases, two different bSSFP datasets were obtained with phase increments ϑ equal to 0 or π (bSSFP$_0$ and bSSFP$_\pi$) respectively, corresponding to the usual implementation of mcDESPOT (18-24, 26, 32).

2.2. Bayesian Analysis of mcDESPOT

Bayesian analysis can be particularly robust for parameter estimation in models with several unknown parameters, especially in the presence of noise (27-31). Unlike NLLS, it does not require initial estimates and so is much less susceptible to problems with local minima. These characteristics arise fundamentally from the process of marginalization over nuisance parameters, defined as those parameters besides the one under current consideration, and are independent of the additional fact that Bayesian inference also provides a natural framework for the incorporation of prior knowledge when available.

Marginalization results in a considerable computational burden, but provides a posterior PDF for each individual parameter. In the case of mcDESPOT, the posterior PDF of f_s follows form:

$$\mathrm{P}(f_s|\mathbf{S}) = \int \frac{\mathrm{P}(\mathbf{\Lambda}^*)L(\mathbf{S}|\mathbf{\Lambda})}{\mathrm{P}(\mathbf{S})}\mathrm{d}\mathbf{\Lambda}^*, \quad [3]$$

where $\mathbf{\Lambda}\left(\mathbf{f_s T_{2,s} T_{2,l} T_{1,s} T_{1,l} M^0_{SPGR} M^0_{bSSFP_0} M^0_{bSSFP_\pi} \sigma_{SPGER} \sigma_{bSSFP_0} \sigma_{bSSFP_\pi}}\right)$ is the vector of unknown parameters, $\boldsymbol{\sigma} = \left(\sigma_{SPGR}\sigma_{bSSFP_0}\sigma_{bSSFP_\pi}\right)$ is the vector of standard deviations, SDs, of the noise, $\mathbf{\Lambda}^*$ is equivalent to $\mathbf{\Lambda}$ but without f_s and represents the vector of nuisance parameters in the determination of f_s, $\mathrm{P}(\mathbf{\Lambda}^*)$ is the product of prior parameter distributions for the elements of $\mathbf{\Lambda}^*$, $\mathrm{P}(\mathbf{S}) = \int \mathrm{P}(\mathbf{\Lambda}^*)\, L(\mathbf{S} \mid \mathbf{\Lambda})\, \mathrm{d}\mathbf{\Lambda}^*$ is a normalization constant, $\mathbf{S} = \left(\mathbf{S}_{SPGR}\mathbf{S}_{bSSFP_0}\mathbf{S}_{bSSFP_\pi}\right)$ is the vector of measured signals, each of which is itself a vector describing the signal amplitude for each value of FA, and $L(\mathbf{S} \mid \mathbf{\Lambda})$ is the joint likelihood function of $\mathbf{S}$ given $\mathbf{\Lambda}$. Given the independent and identically Gaussian distributed elements of $\mathbf{S}$, the joint likelihood function for mcDESPOT is

$$L(\mathbf{S}|\mathbf{\Lambda}) = L(\mathbf{S}_{SPGR}|\mathbf{\Lambda})\, L\left(\mathbf{S}_{bSSFP_0}|\lambda\right) L\left(\mathbf{S}_{bSSFP_\pi}|\boldsymbol{\lambda}\right)$$
$$= \prod_{k=1}^{K} P\left(S^k_{SPGR}|\boldsymbol{\lambda}\right) \prod_{n=1}^{N} P\left(S^n_{bSSFP_0}|\boldsymbol{\lambda}\right) \prod_{n=1}^{N} P\left(S_{bSSFP_\pi}|\boldsymbol{\lambda}\right)$$
$$= \left(\sigma_{SPGR}\sqrt{2\pi}\right)^{-K} \left(\sigma_{bSSFP_0}\sqrt{2\pi}\right)^{-2} \left(\sigma_{bSSFP_\pi}\right)^{-N} \quad exp\left(-\frac{(\mathbf{S}_{SPGR}-\mathbf{M}_{SPGR})(\mathbf{S}_{SPGR}-\mathbf{M}_{SPGR})^T}{2\sigma^2_{SPGR}}\right.$$
$$\left. - \frac{\left(\mathbf{S}_{bSSFP_0}-\mathbf{M}_{bSSFP_0}\right)\left(\mathbf{S}_{bSSFP_0}-\mathbf{M}_{bSSFP_0}\right)^T}{2\sigma^2_{bSSFP_0}} - \frac{(\mathbf{S}_{bSSFP_\pi}-\mathbf{M}_{bSSFP_\pi})(\mathbf{S}_{bSSFP_\pi}-\mathbf{M}_{bSSFP_\pi})^T}{2\sigma^2_{bSSFP_\pi}}\right)$$

where $P(\mathbf{S} \mid \mathbf{\Lambda})$ is the PDF of **S** given **Λ** with obvious subscripting as indicated, the terms of the form (**S** − **M**) are difference of row vectors **S** and **M** across FAs, the superscript T indicates transpose operation, and $\mathbf{M}_{SPGR}$ and $\mathbf{M}_{bSSFP}$ are the row vectors of ideal measurement values at different FAs given by Equations 1 and 2, respectively.

Finally, an estimate, $\hat{f_s}$, of the short fraction, f_s, can be derived as the first moment of its posterior PDF (30) through

$$\hat{f}_s \sqrt{f_s} \mathrm{P}\left(f_s|\mathbf{S}\right) \mathrm{d}f_s, \quad [4]$$

As can be seen from Equations 3 and 4, the estimation of $\hat{f_s}$ requires a high dimensional integration of its posterior PDF in order to perform a complete marginalization over nuisance parameters. One useful technique for reducing the dimensionality of required marginalizations is to use a so-called conjugate prior, by which we mean a prior that can be coupled with a likelihood function to permit analytic closed form integrals over certain nuisance parameters (37). In the following, we describe three different approaches to reduce the dimensionality of parameter space for the estimation of f_s. The first approach is based on data normalization, the second approach on the use of noninformative priors and data normalization, and the final approach on the exclusive use of priors that are noninformative.

2.2.1. Approach 1: Normalized data and known standard deviation of noise—If sufficiently large background regions are available in the SPGR and bSSFP images, σ_{SPGR}, σ_{bSSFP_0} and σ_{bSSFP_π} can be estimated with high accuracy and precision (38), avoiding the need to marginalize over these variables. Further, we can avoid marginalization over $M^0_{SPGR}, M^0_{bSSFP_0}$ and $M^0_{bSSFP_\pi}$ by normalizing both the experimental and theoretical signals by their respective mean values calculated over FAs (18, 24, 26, 32):

$$\tilde{S}^k_{SPGR}=K\frac{S^k_{SPGR}}{\sum_{k=1}^{K}S^k_{SPGR}},\ \tilde{S}^n_{bSSFP_0}=N\frac{S^n_{bSSFP_0}}{\sum_{k=1}^{N}S^n_{bSSFP_0}}\quad\text{and}\quad\tilde{S}^n_{bSSFP_\pi}=N\frac{S^n_{bSSFP_\pi}}{\sum_{k=1}^{N}S^n_{bSSFP_\pi}},\quad\text{and}\quad\tilde{M}^k_{SPGR}=K\frac{M^k_{SPGR}}{\sum_{k=1}^{K}M^k_{SPGR}},\ \tilde{M}^n_{bSSFP_0}=N\frac{M^n_{bSSFP_0}}{\sum_{k=1}^{N}M^n_{bSSFP_0}}\quad\text{and}\quad\tilde{M}^n_{bSSFP_\pi}=N\frac{M^n_{bSSFP_\pi}}{\sum_{k=1}^{N}M^n_{bSSFP_\pi}}$$

. In effect, this further reduces the dimensionality of parameter space from 10 to 4. Equation 3 can be rewritten as

Equation 3 can be rewritten as

$$\begin{aligned}\mathrm{P}\left(f_s|\tilde{\mathbf{S}},\tilde{\sigma}\right)\ =&\left(\tilde{\sigma}_{SPGR}\sqrt{2\pi}\right)^{-K}\left(\tilde{\sigma}_{bSSFP_0}\sqrt{2\pi}\right)^{-N}\left(\tilde{\sigma}_{bSSFP_\pi}\sqrt{2\pi}\right)^{-N}\\&\frac{1}{\mathrm{P}(\tilde{\mathbf{S}})}\sqrt{\frac{1}{\boldsymbol{\lambda}^*}}exp\left(-\frac{\left(\tilde{\mathbf{S}}_{SPGR}-\tilde{\mathbf{M}}_{SPGR}\right)\left(\tilde{\mathbf{S}}_{SPGR}-\tilde{\mathbf{M}}_{SPGR}\right)^T}{2\tilde{\sigma}\sigma^2_{SPGR}}\right.\\&-\frac{\left(\tilde{\mathbf{S}}_{bSSFP_0}-\tilde{\mathbf{M}}_{bSSFP_0}\right)\left(\tilde{\mathbf{S}}_{bSSFP_0}-\tilde{\mathbf{M}}_{bSSFP_0}\right)^T}{2\tilde{\sigma}\sigma^2_{bSSFP_0}}\\&\left.-\frac{\left(\tilde{\mathbf{S}}_{bSSFP_\pi}-\tilde{\mathbf{M}}_{bSSFP_\pi}\right)\left(\tilde{\mathbf{S}}_{bSSFP_\pi}-\tilde{\mathbf{M}}_{bSSFP_\pi}\right)^T}{2\tilde{\sigma}\sigma^2_{bSSFP_\pi}}\right)\mathrm{d}\boldsymbol{\lambda}^*,\end{aligned}\qquad[5]$$

where $\boldsymbol{\lambda}^* = (\ T_{2,s}\ T_{2,l}\ T_{1,s}\ T_{1,l})$ is the vector of the remaining parameters,

$$\frac{1}{\boldsymbol{\lambda}}=\frac{1}{T_{2,s}}\frac{1}{T_{2,l}}\frac{1}{T_{1,s}}\frac{1}{T_{1,l}},\mathrm{d}\boldsymbol{\lambda}^*=\mathrm{d}T_{2,l}\mathrm{d}T_{1,s}\mathrm{d}T_{1,l},\quad\text{and}\quad\tilde{\sigma}_{SPGR}=K\frac{\sigma_{SPGR}}{\sum_{k=1}^{K}S^k_{SPGR}},\quad\tilde{\sigma}_{bSSFP_0}=N\frac{\sigma_{bSSFP_0}}{\sum_{n=1}^{N}S^0_{bSSFP}}\quad\text{and}\quad\tilde{\sigma}_{bSSFP_\pi}=N\frac{\sigma_{bSSFP_\pi}}{\sum_{n=1}^{N}S^\pi_{bSSFP}}$$

represent the normalized SDs of the noise. In the present study, the number of measurements s much greater than the number of derived parameters, so that results are largely independent of reasonable selections of prior probabilities (37). We assumed a form of noninformative Jeffreys priors, that is, $\mathrm{P}(\boldsymbol{\lambda}^*) = 1/\boldsymbol{\lambda}^*$ with obvious notation for multiplication of parameter reciprocals (27-28, 39).

2.2.2. Approach 2: Normalized data and unknown standard deviation of noise: Jeffreys priors σ—We now describe the analysis for the case in which there is insufficient background in the SPGR and bSSFP images to ensure accurate estimation of the noise SD. We again assume Jeffreys priors on $\boldsymbol{\sigma}$, so that $\mathrm{P}(\boldsymbol{\sigma})=\frac{1}{\sigma_{SPGR}}\frac{1}{\sigma_{bSSFP_0}}\frac{1}{\sigma_{bSSFP_\pi}}$ with the same

assumption on $\boldsymbol{\lambda}^*$ as above. Then, using

$\int_0^\infty y^{-a/2} exp\left(-\frac{b}{2y}\right) \quad dy \quad = \Gamma\left(\frac{a-2}{2}\right)\left(\frac{2}{b}\right)^{(a-2)/2}$, where Γ is the gamma function, Equation 3 for the posterior PDF of f_s becomes (see Appendix)

$$\begin{aligned} P\left(f_s|\tilde{\mathbf{S}}\right) \quad = & \frac{\Gamma K/2)\Gamma(N/2)\Gamma(N/2)}{8\sqrt{\pi^K}\sqrt{\pi^N}\sqrt{\pi^N}} \int \frac{1}{P\left(\tilde{\mathbf{S}}\right)} - \frac{1}{\boldsymbol{\Lambda}^*} \left(\left(\tilde{\mathbf{S}}_{SPGR} - \tilde{\mathbf{M}}_{SPGR}\right)\left(\tilde{\mathbf{S}}_{SPGR} - \tilde{\mathbf{M}}_{SPGR}\right)^T\right)^{\frac{K}{2}} \left(\left(\tilde{\mathbf{S}}_{bSSFP_0}\right.\right. \\ & \left.\left. - \tilde{\mathbf{M}}_{bSSFP_0}\right)\left(\tilde{\mathbf{S}}_{bSSFP_0} - \tilde{\mathbf{M}}_{bSSFP_0}\right)^T\right)^{-\frac{-N}{2}} \left(\left(\tilde{\mathbf{S}}_{bSSFP_\pi}\right.\right. \\ & \left.\left. - \tilde{\mathbf{M}}_{bSSFP_\pi}\right)\left(\tilde{\mathbf{S}}_{bSSFP_\pi} - \tilde{\mathbf{M}}_{bSSFP_\pi}\right)^T\right)^{-\frac{N}{2}} d\boldsymbol{\lambda}^*, \end{aligned} \quad [6]$$

where again, $\boldsymbol{\lambda}^* = (\ T_{2,s}\ T_{2,l}\ T_{1,s}\ T_{1,l}\ )$. As can be seen from Equation 6, the combination of the Jeffreys priors and the Gaussian likelihood functions permitted us to obtain a posterior PDF of f_s, $P(f_s \mid \tilde{\mathbf{S}})$, that is independent of σ_{SPGR}, σ_{bSSFP_0} and σ_{bSSFP_π}, eliminating the need to marginalize over these variables. As in the above, the experimental and the theoretical signals were normalized in order to avoid marginalization over $M^0_{SPGR}, M^0_{bSSFP_0}$ and $M^0_{bSSFP_\pi}$. Therefore, the dimensionality of the parameter space is again reduced from 10 to 4.

2.2.3. Approach 3: Non-normalized data and unknown standard deviations of the noise: NIG priors on $\mathbf{M_0}$ and $\boldsymbol{\sigma}$—Normalization with respect to the mean of the measured data as described above may introduce a bias due to the potential propagation of uncertainties in these mean values due to noise, especially in the case of a limited number of measurements. To overcome this potential limitation, we also address the case of non-normalized data with unknown noise SD using conjugate priors that permit closed-form solutions. For this, conjugate normal-inverse-Gamma distributions, NIG($\mathbf{M}_0$, $\mathbf{M}^2$), on $\mathbf{M}_0$ and $\boldsymbol{\sigma}$, given by

$$\mathrm{NIG}\left(\mathbf{M}_0, \boldsymbol{\sigma}^2\right) = \mathrm{NIG}\left(M^0_{SPGR}, \sigma^2_{SPGR}\right)\mathrm{NIG}\left(M^0_{bSSFP_0}, \sigma^2_{bSSFP_0}\right)\mathrm{NIG}\left(M^0_{bSSFP_\pi}, \sigma^2_{bSSFP_\pi}\right).$$

were taken as priors (40). Thus, our prior distributions were given by

$$\mathrm{NIG}\left(M_0, \sigma^2|V, \alpha, \beta\right) = \mathrm{N}\left(0|V\sigma^2\right)\mathrm{IG}\left(\sigma^2|\alpha\beta\right) = \sqrt{\frac{V}{2\pi}}\frac{\beta^\alpha}{\Sigma(\alpha)}\left(\frac{1}{\sigma^2}\right)^{2\alpha+3} exp\left(-\frac{2\beta + VM_0^2}{2\sigma^2}\right),$$

where $N(0 \mid V\sigma^2)$ is a normal distribution over M_0 with zero mean and variance $V\sigma^2$, with $V = \delta(\mathbf{g}\,\mathbf{g}^T)$, where $\mathbf{g}$ represents the vector of theoretical signal measurements and δ is a scale parameter, with large δ indicating a minimally-informative prior. $IG(\sigma^2 \mid \alpha, \beta)$ is an inverse Gamma prior on σ^2 with shape parameter α and scale parameter β, with small values of α and β indicating a minimally-informative prior. A detailed description of the NIG prior can be found in (30, 40-41). The combination of the NIG prior distributions with their corresponding Gaussian likelihood functions allows one to obtain a closed form of

marginalized joint likelihood function, $L(\mathbf{S} \mid \boldsymbol{\lambda})$, which is explicitly independent of $\mathbf{M}_0$ and $\boldsymbol{\sigma}$ through

$$L(\mathbf{S}|\boldsymbol{\lambda}) = \int \mathrm{NIG}(\mathbf{M}_0, \boldsymbol{\sigma}^2)\, L(\mathbf{S}|\boldsymbol{\Lambda})\, \mathrm{d}\boldsymbol{\sigma}^2$$
$$C\left(\left(\mathbf{S}_{SPGR}\mathbf{S}_{SPGR}{}^T\right) - \frac{\left(\mathbf{g}_{SPGR}\mathbf{S}_{SPGR}{}^T\right)^2}{\left(\mathbf{g}_{SPGR}\quad \mathbf{g}_{SPGR}{}^T\right)}\right)^{-\frac{K}{2}} \left(\left(\mathbf{S}_{bSSFP_0}\mathbf{S}_{bSSFP_0}{}^T\right) \frac{\left(\mathbf{g}_{bSSFP_0}\mathbf{S}_{bSSFP_0}{}^T\right)^2}{\left(\mathbf{g}_{bSSFP_0}\quad \mathbf{g}_{bSSFP_0}{}^T\right)}\right)^{-\frac{N}{2}} \left(\left(\mathbf{S}_{bSSFP_\pi}\mathbf{S}_{bSSFP_\pi}{}^T\right) \frac{\left(\mathbf{g}_{bSSFP_\pi}\mathbf{S}_{bSSFP_\pi}{}^T\right)^2}{\left(\mathbf{g}_{bSSFP_\pi}\quad \mathbf{g}_{bSSFP_\pi}{}^T\right)}\right)^{-\frac{N}{2}}$$

where $\boldsymbol{\lambda} = (f_2\ T_{2,s}\ T_{2,l}\ T_{1,s}\ T_{1,l})$, $\mathrm{d}\mathbf{M}_0 = \mathrm{d}M_0^{SPGR}\mathrm{d}M_0^{bSSFP_0}\mathrm{d}M_0^{bSSFP_\pi}$ $\mathrm{d}\boldsymbol{\sigma}^2 = \mathrm{d}\sigma^2_{SPGR}\mathrm{d}\sigma^2_{bSSFP_0}\mathrm{d}\sigma^2_{bSSFP_\pi}$ C is a proportionality constant that depends only on a, β, δ, K and N and is independent of $\boldsymbol{\lambda}$, $\mathbf{g}_{\mathbf{SPGR}} = \sin\boldsymbol{\alpha}\left(\mathbf{f_s}\frac{\mathbf{1}-\mathbf{E_{1,s}}}{\mathbf{1}-\mathbf{E_{1,s}}\cos\boldsymbol{\alpha}} + (\mathbf{1}-\mathbf{f_s})\frac{\mathbf{1}-\mathbf{E_{1,l}}}{\mathbf{1}-\mathbf{E_{1,l}}\cos\boldsymbol{\alpha}}\right)$ and $\mathbf{g}_{\mathbf{bSSFP}} = \left|\left(f_s\left(\mathbf{M}_{a,s}+i\mathbf{M}_{b,s}\right) + (1-f_s)\left(\mathbf{M}_{a,l}+i\mathbf{M}_{b,l}\right)\right)\right|$, where $\mathbf{M}_a$ and $\mathbf{M}_b$ were defined in Equation 2. Therefore, the posterior PDF of f_s given by Equation 3 can be rewritten as

$$\mathrm{P}(f_s|\mathbf{S}) = \frac{1}{\mathrm{P}(\mathbf{S})}\int \frac{1}{\lambda^*} L(\mathbf{S}|\boldsymbol{\lambda})\, \mathrm{d}\boldsymbol{\lambda}^*, \quad [7]$$

where, again, $\boldsymbol{\lambda}^* = (\ T_{2,s}\ T_{2,l}\ T_{1,s}\ T_{1,l})$. As can be seen from Equation 7, this third approach also permits reduction of the dimensionality of the parameter space from 10 to 4.

2.3. Bayesian Monte Carlo Analysis of mcDESPOT

Although the dimensionality of the parameter space is considerably reduced using the Bayesian analyses described above, the estimation of f_s still requires a four dimensional integration of the posterior PDF defined in Equation 4, as indicated in Equations 5-7. This remains an intractable high dimensional integration requiring extensive computational time. To overcome this difficulty, rather than standard fully sampled integrations, we explored the use of standard Monte Carlo (MC) integration (42). In brief, MC integration is performed by averaging the values of the integrand, the posterior PDF defined in Equation 5, over a large random set, M, of parameter combinations. By assuming random sampling from a uniform PDF on a grid defined over the integration parameter ranges, the posterior PDF of f_s can be approximated as

$$\mathrm{P}(f_s|\mathbf{S}) \simeq \frac{V}{M}\sum_{m=1}^{M}\frac{\mathrm{P}(\lambda^*_{\mathbf{m}})\, L(\mathbf{S}|\boldsymbol{\lambda}_m)}{\mathrm{P}(\mathbf{S})}, \quad [8]$$

where V is a volume constant. In the following, we will refer to this method as Bayesian Monte Carlo (BMC).

3. MATERIALS and METHODS

3.1. Simulation Analysis

3.1.1. Input Parameters, Parameter Bounds, and SNR Definition—The following input parameters were used for all simulations: $TR_{SPGR} = TR_{bSSFP} = 6.5$ ms, $\alpha_{SPGR} = [2\ 4\ 6\ 8\ 10\ 12\ 14\ 16\ 18\ 20]°$, $\beta_{bSSFP} = [2\ 6\ 14\ 22\ 30\ 38\ 46\ 54\ 62\ 70]°$, with two bSSFP datasets generated with RF phase increments of 0 or π. The limits of the parameter search space for the SRC-NLLS algorithm were: $0 \leq f_s \leq 1$, 2 ms $\leq T_{2,s} \leq$ 45 ms, 45 ms $\leq T_{2,l} \leq$ 200 ms, 100 ms $\leq T_{1,s} \leq$ 700 ms and 700 ms $\leq T_{1,l} \leq$ 3000 ms. These values were also used as limits of the integrals needed in the fully sampled Bayesian marginalization (Eqs. 5-7) and as ranges for the random sampling needed in the BMC integration (Eq. 8). Details of the SRC-NLLS algorithm can be found in (25-26). Briefly, for each iteration, 20,000 random samples were generated within the specified parameter bounds. The 50 solutions with the lowest least-squares residuals (LSR) were used to construct the bounds of the next iteration. Iterations were terminated after convergence was achieved, defined as a relative difference between the minimum and maximum values of all parameters of less than 1%, or after 30 iterations.

Zero-mean Gaussian white noise of SD σ was added to simulated signals in order to investigate results across a range of SNR, defined as SNR = M_0 / σ, where M_0 represents the signal amplitude at TE = 0 ms. All numerical calculations were performed with MATLAB (MathWorks, Natick, MA, USA).

3.1.2. Comparisons of the BMC and Fully Sampled Integrations—Input parameter values of $T_{2,s} = 15$ ms, $T_{2,l} = 100$ ms, $T_{1,s} = 450$ ms and $T_{1,l} = 1800$ ms were used in the following analyses, and were selected based on values obtained in human brain studies (10-12, 14-16, 18-21).

Determination of the optimal total number of samples for the BMC integration: In order to define a value for the number of random samples, M, used in the BMC integration (Eq. 8) that maximizes integration accuracy in the determination of f_s while maintaining reduced computational time, estimations of f_s were performed for different values of M between 10 and 100,000. Analyses were performed for an input f_s value of 0.15 and two SNR values of 500 and 2000. For each combination of SNR and M, results are presented as the mean-squared-error, MSE, that incorporates information about both bias and dispersion (38). MSE was calculated as the difference between the true value, f_s, used in generating the MR signal, and estimated values, $\hat{f}_s^{BMC}$, obtained using BMC integration, according to

$$\mathrm{MSE} = R^{-1} \sum_{r=1}^{R} \left(f_s - \hat{f}_{s,r}^{BMC} \right)^2, \quad [9]$$

where R, the total number of noise realizations, was fixed at $R = 1001$. Analyses were performed for all three Bayesian-based approaches described above.

Comparison of the BMC and fully sampled integrations: The BMC (Eq. 8) and fully sampled (Eq. 5) integration techniques for the estimation of f_s were compared for f_s values

of 0.05, 0.15 and 0.3 at SNR values of 500, 1000 and 2000. For each SNR and f_s combination, BMC integration was performed with M = 20,000, which was determined to be an optimal value from the analysis described above. Results are presented as the mean, SD, and mean relative error, MRE, in estimated f_s values over 1001 noise realizations. The MRE were calculated as the difference between estimated values obtained using fully sampled, $\hat{f}_{FS}^{s}$, and BMC, $\hat{f}_{s}^{BMC}$, integrations through

$$\mathrm{MRE}\,(\%) = \frac{100}{R}\sum_{r=1}^{R}\frac{|\hat{f}_{s,r}^{FS} - \hat{f}_{s,r}^{BMC}}{\hat{f}_{s,r}^{FS}}, \quad [10]$$

where R is the total number of noise realizations. MRE was used instead of MSE, as defined above, in order to assess relative error for different values of f_s. Extensive simulations demonstrated that the three Bayesian approaches showed very similar performance, so that results for the comparison of BMC and fully sampled integrations are shown for the first approach only (Eq. 5).

3.1.3. Comparison of the SRC Algorithm and the BMC Approaches—

Comparison of the SRC- and BMC-mcDESPOT methods for the estimation of f_s were evaluated using numerical simulations. The first evaluation was performed for different f_s values of 0.05, 0.1, 0.15, 0.2, 0.3 and 0.5 at SNR values of 500, 1000 and 2000, where the other underlying input parameters were fixed at $T_{2,s}$ = 15 ms, $T_{2,l}$ = 100 ms, $T_{1,s}$ = 450 ms and $T_{1,l}$ = 1800 ms. The second evaluation was performed by fixing the f_s and SNR values to 0.15 and 500, respectively, and exploring several values of the remaining parameters, with $T_{2,s}$ = (10, 15, 20, 25) ms, $T_{2,l}$ = (70, 100, 110, 150) ms, $T_{1,s}$ = (300, 400, 450, 550) ms and $T_{1,l}$ = (1400, 1800, 2000, 2500) ms.

For each parameter combination and SNR, the performance of each method was evaluated by calculating the relative bias, relative dispersion and relative root-mean-squared-error, RMSE, in the estimation of f_s (43). The relative bias, a measure of accuracy, was defined as

$$\mathrm{Bias}\,(\%) = 100 * \frac{|f_s - \overline{\hat{f}}_s|}{f_s}, \quad [11]$$

where $\overline{\hat{f}}_s = (1/R)\sum_{r=1}^{R}\hat{f}_s^r$ and R is the total number of noise realizations, R = 1001. The relative dispersion, a measure of precision, was defined as

$$\mathrm{Dispersion} \quad (\%) = 100 * \frac{\sqrt{(1/(R-1))\sum_{r=1}^{R}\left(\hat{f}_s^r - \hat{f}_s\right)}}{f_s}, \quad [12]$$

and finally the RMSE, a measure including both precision and accuracy (38), was defined as the root-square of the sum of the squared relative bias of the estimator and its relative variance by the expression

$$\text{RMSE} \quad (\%) = \sqrt{\text{Bias}^2 + \text{Dispersion}^2}. \quad [13]$$

3.1.4. Energy Surface and Posterior PDF Analyses—For NLLS, including SRC-NLLS, the least-squares energy surface structure defines in part the reliability of parameter fits. In contrast, for Bayesian analysis, reliability of estimates are defined by the derived posterior PDFs. Therefore, to characterize the SRC-NLLS analysis, minimum LSR (MLSR) was calculated as a function of f_s by fixing f_s to a given value and varying all other parameters. The LSR was calculated over the entire combined multidimensional range of these other parameters for each fixed value of f_s, with the minimum calculated LSR designated as the MLSR. This process was repeated for different fixed values of f_s (24). For the BMC analyses, the posterior PDF of f_s was calculated by fixing f_s to a given value and marginalizing over all remaining parameters as described above. This process was again repeated for different fixed values of f_s. In both cases, the signal was generated with underlying input parameters of $T_{2,s}$ = 15 ms, $T_{2,l}$ = 100 ms, $T_{1,s}$ = 450 ms and $T_{1,l}$ = 1800 ms, with noise added as described above. All analyses were performed for f_s values of 0.15 and 0.3 and with SNR of 500.

3.2. Experimental Analysis

3.2.1. Data Acquisition—All MRI experiments were performed on a 3T whole body MRI Philips system (Achieva, Best, The Netherlands) using the internal quadrature body coil for transmission and an eight-channel phased-array head coil for reception. Data were collected from the brain of a 23 year-old healthy female, from whom written informed consent was obtained prior to participation. All examinations were performed with approval of the local institutional review board.

Three separate sets of acquisition and reconstruction parameters were used to generate mcDESPOT data with a range of SNR and spatial resolution (SR). We selected oblique imaging slices that contained well-recognized and well-represented white and grey matter, as well as clear delineation of ventricles. The oblique slice package was centered on a plane roughly 4 cm superior to the external auditory meatus. In the SNR_{High} protocol, that with the highest SNR, all SPGR and bSSFP datasets were acquired with 4 signal averages (SA) and with SR = 1 × 1 × 3 mm^3, and then reconstructed to SR = 0.45 × 0.45 × 3 mm^3. In the $\text{SNR}_{\text{Intermediate}}$ protocol, with intermediate SNR datasets, SPGR and bSSFP datasets were acquired with 1 SA and SR = 1 × 1 × 3 mm^3, reconstructed to SR = 0.45 × 0.45 × 3 mm^3. In the SNR_{Low} protocol, with the lowest SNR, SPGR and bSSFP datasets were acquired with 1 SA and SR = 1 × 1 × 1 mm^3 and reconstructed to SR = 0.45 × 0.45 × 1 mm^3. For each of these three protocols, the 3D SPGR images were acquired with FAs α_{SPGR} = [2 4 6 8 10 12 14 16 18 20]°, with TE_{SPGR} = 1.6 ms and TR_{SPGR} = 6.6 ms, while the 3D bSSFP images were acquired with FAs β_{bSSFP} = [2 6 14 22 30 38 46 54 62 70]°, with TE_{bSSFP} = 3.3 ms and TR_{bSSFP} = 6.6 ms. For all datasets, the bSSFP images were acquired twice, once with $\Delta\omega$ = 0 Hz (*i.e.* bSSFP_{π}) and once with $\Delta\omega$ = 1/(2 * TR) = 76 Hz (*i.e.* bSSFP_0), with, in both cases, $\vartheta = \pi$. All images were obtained with field of view (FOV) = 200 × 200 × 9 mm^3.

Further, SPGR and bSSFP images with a null FA were acquired for each protocol and used to estimate the noise SD needed for BMC1.

In this *in-vivo* study, the SNR was defined as (44-45)

$$\mathrm{SNR}=\frac{\sqrt{\bar{S}_{SPGR}(\alpha_{SPGR}=8^o)^2-2L\hat{\sigma}^2(\alpha_{SPGR}=0^o)}}{\hat{\sigma}(\alpha_{SPGR}=0^o}},$$

where $L = 8$ is the total number of channels of the phased-array head coil and $\bar{S}_{SPGR}(\alpha_{SPGR} = 8°)^2$ was calculated as the square of the mean signal from all regions in the SPGR image obtained with $\alpha_{SPGR} = 8°$ corresponding to the maximum signal image in the regions over which the MWF maps were calculated (See Data Analysis section). In addition, $\hat{\sigma}(\alpha_{SPGR}=0^o)$ is the noise SD calculated through $\hat{\sigma}(\alpha_{SPGR}=0^o)=\sqrt{\bar{S}^2_{SPGR}(\alpha_{SPGR}=0^o)/2L}$, where $\bar{S}^2_{SPGR}(\alpha_{SPGR}=0^o)$ is the mean of the squared pixel intensity values calculated from a large region in the SPGR image obtained with $\alpha_{SPGR} = 0°$ (44). The $\mathrm{SNR_{High}}$, $\mathrm{SNR_{Intermediate}}$ and $\mathrm{SNR_{Low}}$ values calculated for each protocol described above were ~90, ~40 and ~25, respectively.

For the B_1 calibration needed for mcDESPOT (32), the S-DAM method (35) was used. Two 3D images with excitation FAs of 70° and 140° were acquired, with SR = 2 × 2 × 3 $\mathrm{mm^3}$, and then reconstructed to SR = 0.45 × 0.45 × 3 $\mathrm{mm^3}$ for both $\mathrm{SNR_{High}}$ and $\mathrm{SNR_{Intermediate}}$ protocols, or to SR = 0.45 × 0.45 × 1 $\mathrm{mm^3}$ for $\mathrm{SNR_{Low}}$ protocol. The other acquisition parameters were: FOV = 200 × 200 × 9 $\mathrm{mm^3}$, $\mathrm{TE}_{S\text{-}DAM}$ = 1.73 ms and $\mathrm{TR}_{S\text{-}DAM}$ = 1538 ms.

3.2.2 Data Analysis—Images from each of the three mcDESPOT datasets with different SNR and SR, as described above, were analyzed on a voxel-wise basis. First, the S-DAM datasets were used to generate B_1 maps. These were then used to generate T_1 maps through a fit of the SPGR data as a function of FAs to a functional form incorporating only a single underlying component. Similarly, T_2 and $\Delta\omega$ * TR maps were then generated according to the $\mathrm{DESPOT_2}$-FM method (36) by fitting the bSSFP datasets as a function of FA to a single component form of the signal, using the voxel-wise B_1 and T_1 values obtained as outlined above. Finally, the $\Delta\omega$ * TR and B_1 maps, combined with the SPGR and bSSFP datasets, were used to generate f_s maps reflecting MWF (18-23).

For each mcDESPOT dataset, MWF maps were generated using the SRC-NLLS algorithm and the BMC approaches as described above. To correspond to actual practice (24, 26, 46), the boundary conditions for the SRC-NLLS algorithm were set to $0 \le f_s \le 0.6$, 2 ms $\le T_{2,s} \le$ 45 ms, 75 ms $\le T_{2,l} \le$ 200 ms, 100 ms $\le T_{1,s} \le$ 700 ms and 700 ms $\le T_{1,l} \le$ 3000 ms. The same boundary conditions were used as sampling ranges for BMC. Further, manual segmentation was performed to eliminate ventricles and non-brain regions of the images, with statistical analyses and MWF maps generated for the remaining regions of interest. The statistical analyses, consisting of calculations of the mean, SD, and coefficient of variation, CoV, for the pixel-wise estimate of MWF, were performed on three different image regions as indicated in Figure 9. The first region encompasses the frontal lobes, the second region

encloses the temporal lobes, and the third region encloses the occipital lobes. For each region, all the statistical analyses were calculated from pixels with MWF > 1% defined from the MWF maps generated using BMC3 approach. Finally, MLSR and posterior PDF analyses were performed on a single voxel from data obtained with the SNR_{Low} dataset as described in the Simulation Analysis section above.

4. RESULTS

4.1. Simulation Analysis Results

The effect of varying the number of random samples used in BMC integration—Figure 1 shows the MSE, as defined in Equation 9, for estimation of the short fraction, f_s, as a function of the total number of samples, M, used in the BMC integration (Eq. 8). Results are presented for SNR values of 500 and 2000 using the three different BMC approaches described in the Materials and Methods section. For each of the three and for both values of SNR, the MSE decreased with increasing M, as expected. However, minimal further decrease in MSE as a function of M was seen for $M \simeq 6000$ for SNR = 500, and for $M \simeq 10000$ for SNR = 2000, indicating that, as expected, higher SNR permits further refinement of the accuracy of the integration through use of additional sampled points.

Accuracy of f_s determination as a function of SNR for BMC compared to fully sampled integration—Figure 2 shows the mean, SD and MRE, as defined in Equation 10, for the estimation of f_s calculated over 1001 noise realizations using fully sampled (Eq. 5) or BMC (Eq. 8) integration for three different f_s and SNR combinations. As is evident, BMC integration provides results that are virtually indistinguishable from those obtained with the fully sampled integration. In spite of the large number of randomly sampled points used for BMC integration, processing time was reduced to a few minutes from the several hours required for the fully sampled integration.

Comparison of the accuracy of SRC-NLLS and BMC—Figure 3 shows the relative bias, dispersion and RMSE in the estimation of f_s for several combinations of SNR and true input f_s values. As expected, relative bias, dispersion and RMSE decreased with increasing SNR or f_s values in all cases. Comparing the methods, the BMC approaches demonstrated a substantial reduction of relative bias, dispersion and RMSE compared to the SRC-NLLS algorithm, especially at low-to-moderate SNR (*i.e.* SNR < 2000). However, at high SNR, the SRC-NLLS was able to perform, overall, almost as well as the BMC, especially for $f_s \geq 0.15$, that is, with more equal component fractions. In addition, at low SNR (*i.e.* SNR < 1000), BMC3 showed a slight overall decrease in relative bias, dispersion and RMSE compared to BMC1 and BMC2. Using average values over all parameter combinations as a benchmark for performance, the averaged values for relative bias were 18/4/4/4%, for relative dispersion 44/24/25/24% and for RMSE 48/24/25/24% for SRC-NLLS, BMC1, BMC2 and BMC3, respectively, indicating the superior performance of BMC analysis. For SNR = 500, the mean computation times over several noise realizations for the calculation of f_s using a 2.4 GHz computer for SRC-NLLS and for each of the BMC were ~0.6 ms and ~1.7 ms, respectively, with the computation time for the three BMC analyses being essentially identical.

Figure 4 shows the relative bias, dispersion and RMSE in the estimation of f_s using SRC-NLLS and BMC analyses. Results were obtained by fixing the f_s and SNR values to 0.15 and 500, respectively, and varying the values of the remaining, nuisance, parameters. In all cases, the relative dispersion and RMSE of estimated f_s values varied minimally with respect to the values of the nuisance parameters. Although the variation in relative bias was greater, it nevertheless remained relatively small for all BMC methods, between 2% and 13%, as compared to the SRC-NLLS, for which bias ranged between 12% and 44%. These results showed that the undesired dependence on the derived value of f_s on nuisance parameters is considerably attenuated through use of Bayesian marginalization. For all parameter combinations investigated, the Bayesian approaches demonstrated substantially reduced relative bias, dispersion and RMSE as compared to the SRC-NLLS algorithm. We found values for relative bias of 32/5/5/4%, for relative dispersion 69/30/31/28%, and for RMSE 76/30/32/28% for the SRC-NLLS, BMC1, BMC2 and BMC3, respectively, again indicating the substantial improvement in the quality of estimates of f_s through use of BMC integration.

Reliability measures of estimates of f_s for SRC-NLLS and BMC—Figure 5 shows the histogram of f_s estimates obtained from 1001 noise realizations using SRC-NLLS and BMC analyses (top row), and the MLSR and posterior PDF for f_s obtained for a single noise realization as a function of f_s (middle and bottom rows, respectively). Results were obtained from signals generated with SNR = 500. It is clear from the histograms that the bias and dispersion in f_s estimates were much greater for SRC-NLLS than for the BMC. The MLSR and posterior PDF illustrations indicate the underlying basis for the superior performance of the Bayesian methods as compared to SRC-NLLS. As is readily seen, the MLSR curves for f_s exhibit an extensive flat region extending on either side of the true input f_s values. In contrast, the posterior PDF of f_s is sharply peaked around the true input f_s value.

4.2. Experimental Analysis Results

B_1 and off-resonance frequency, $\Delta\omega$, mapping from noisy images—Figure 6 shows representative bSSFP and SPGR images and corresponding calculated B_1 and $\Delta\omega^*$ TR maps for each of the three SNR protocol acquisitions. The impact of SNR is readily seen, with small anatomic structures, such as blood vessels and white-grey matter boundaries, increasingly obscured for decreasing SNR. Nevertheless, for each of the three levels of SNR, high quality B_1 and $\Delta\omega^*$ TR parameter maps were derived through a mono-component fit. Further, the calculated B_1 and $\Delta\omega^*$ TR maps clearly demonstrate the spatial extent and the degree of RF inhomogeneity and off-resonance effects, respectively.

Qualitative and quantitative comparison of MWF maps derived using SRC-NLLS and BMC as a function of SNR—Figure 7 shows f_s parameter maps, reflecting MWF, derived from the *in-vivo* brain images obtained with the SNR_{High}, $SNR_{Intermediate}$ and SNR_{Low} protocols using SRC-NLLS, and BMC1, BMC2, and BMC3 analyses. At SNR_{High}, all methods performed well, but with superior performance demonstrated with BMC2 and BMC3 as compared to BMC1 and SRC-NLLS. This is evidenced by the much more homogenous MWF maps for BMC2 and BMC3. For the lower SNR datasets (Figs. 7-8), both SRC-NLLS and BMC1 results show substantial random variation in estimated MWF in several image regions, while BMC2 and BMC3 performed similarly and produced much

higher quality MWF maps. This is clearly seen from Figure 8 showing MWF calculated from different slices of the SNR_{Low} dataset. To examine this quantitatively, the mean, SD and CoV of the estimates of MWF were calculated for three different brain regions corresponding to the frontal, temporal and occipital lobes, as shown in Fig 9. In each case, although the mean values varied little with decreasing SNR, both SD and CoV increased with decreasing SNR. The results clearly indicate the superior overall performance of BMC2 and BMC3 as compared to BMC1 and SRC-NLLS.

Reliability measures of estimates of MWF for SRC-NLLS and BMC—Figure 10 shows the MLSR obtained through SRC-NLLS and the Bayesian posterior PDF of MWF as a function of MWF, that is, of f_s, for the SNR_{Low} brain data shown in Figure 7. As is readily seen, the MLSR curve for MWF exhibits an extensive flat region. In contrast, the posterior PDF of MWF is peaked around a unique MWF value. These results correspond to the simulation results shown in Figure 5.

5. DISCUSSION

5.1. BMC *vs.* SRC-NLLS

We investigated three different implementations of Bayesian probability analyses for the estimation of the short-T_2 fraction, f_s, representing MWF, from the two-component mcDESPOT signal model. BMC1 uses normalization by average signal amplitude, and assumes that noise can be accurately estimated from signal-free regions of the image. BMC2 likewise uses average amplitude normalization, but incorporates a full treatment of noise as an unknown variable through marginalization. BMC3, the most general approach, does not use amplitude normalization and incorporates marginalization over both noise and signal amplitude.

We evaluated the performance of these implementations numerically over wide ranges of SNR and underlying input parameter values, and experimentally from MR imaging data of human brain obtained through use of three different protocols reflecting different noise levels and spatial resolutions. The accuracy and precision in the estimation of f_s (or MWF) obtained with each of the three BMC analyses were systematically compared to those obtained using the SRC-NLLS algorithm, conventionally used for parameter estimation from mcDESPOT. Overall, we found greatly improved accuracy and precision in the estimation of f_s, that is MWF, using the BMC as compared to the SRC-NLLS, especially at lower-to-moderate SNRs (Figs. 3-4 and 7-9). This may be attributable to several facts. First, in contrast to SRC-NLLS, noise SD was either explicitly (BMC1) or implicitly (BMC2 and BMC3) incorporated into the BMC approaches. In addition, in the Bayesian analyses, the parameter of interest, f_s (or MWF), is estimated independently through marginalization over all values of the remaining nuisance parameters. This is in contrast to the SRC-NLLS algorithm in which all unknown parameters are estimated simultaneously. This leads to potential difficulties with local minima, especially in higher-dimensional problems (24). Fundamentally, this arises from the multiple compensating degrees of freedom available through the various parameters, so that different parameter combinations can result in

nearly-equivalent LSR. This is reflected in the flattening of the energy surface of MLSR (Figs. 5 and 10) seen with increasing model complexity (24).

Our results are in agreement with the previous work of Neil and Bretthorst (27) and Bouhrara *et al.* (31) which showed improved accuracy and precision in the estimation of the diffusion and transverse relaxation parameters, respectively, from two-component signal models through use of Bayesian-based approaches compared to NLLS-based methods. In addition, the Bayesian analysis that we have outlined is widely applicable and has great potential to improve the quality of derived MWF from other MRI techniques, such as gradient recalled echo- or other steady state-based analyses (47-49, 50).

In the present work, we based our analysis on the conventional SPGR and bSSFP signal models (Eqs. 1-2) incorporated into mcDESPOT. These models ignore the transverse signal decay that occurs during the time between the preceding pulse and the echo formation in SPGR, and underestimates the bSSFP signal by neglecting the fact that echo formation occurs at a time $TR_{bSSFP}/2$, rather than TR_{bSSFP}, after the pulse that precedes acquisition. This neglect of finite TE effects can introduces bias in parameter estimates, especially for data obtained with relatively long TEs (24, 51). However, the focus of the present work was to analyze the mcDESPOT method as usually implemented.

5.2. BMC Analysis

Our simulations showed that the performance of the three BMC methods investigated here were very similar with, in general, a slightly improved accuracy and precision found using BMC3 (Figs. 3-4). We attribute this to the fact that, unlike BMC3, BMC1 and BMC2 use normalization with respect to the mean amplitude of noisy data. Errors in the calculation of this mean due to noise may introduce a bias in the derivation of the remaining signal parameters, including f_s (or MWF), especially in the case of a limited number of measurements. In our study, the mean amplitude was calculated over a large number of data points, so that the improved accuracy and precision using BMC3 was marginal.

In this work, all priors were taken as noninformative in order to avoid introducing biases into the derived posterior PDF. In addition, the likelihood functions were the dominant terms in the posterior PDFs, so that use of conjugate priors also resulted in negligible bias, as seen from our results. These results motivate investigation of other forms of prior probabilities, such as spatial priors (30), which may further reduce the dispersion seen in the derived MWF maps at low SNR (Figs. 7-8).

Comparison of the three BMC methods was performed under the assumption that the correct values of σ_{SPGR}, σ_{bSSFP0} and $\sigma_{bSSFP\pi}$, needed for BMC1, are known precisely in the numerical simulations. However, the quality of the estimate of f_s, that is, MWF, will depend upon the quality of the estimates $\hat{\sigma}_{SPGR}$, $\hat{\sigma}_{bSSFP_0}$ and $\hat{\sigma}_{bSSFP_\pi}$. Simulation analysis (Table 1) indicates that, as expected, moderate errors (≤ 20%) in the estimated values of noise parameters, such as would be the case for estimation from large background regions of the images (38, 52), have a negligible impact on parameter estimates. Further, the *in-vivo* analyses highlighted the limited performance of BMC1 due to the lack of spatial invariance of the noise (Fig. 11), likely due to the correlation between the channels of the phased-array

coil. This spatial variation of noise may explain the inferiority of parameter estimates from BMC1 as compared to BMC2 and BMC3 for the *in-vivo* analyses (Fig. 7-9). This problem may be addressed through use of techniques that consider the non-uniformity of noise (53).

In this work, we assumed a Gaussian noise distribution. This allowed us to obtain closed form expressions for marginalized likelihood functions, thereby reducing the required integrations. However, it is well-known that the noise in magnitude MR images can be described by a Gaussian distribution only for SNR >~ 3 (43, 54), which is therefore a required approximation for the applicability of our specific results. However, the extension of BMC1 to the case of Rician or, more generally, non-central-chi distributed noise, as is appropriate for multiple receive coils (44-45), is straightforward through appropriate modification of the likelihood function given by Equation 4. In contrast, application of BMC2 and BMC3 as implemented here for non-Gaussian noise would require construction of appropriate priors to permit derivation of closed form expressions for marginalized likelihood functions. Lacking this, the required integrations could, in principle, be performed numerically.

BMC integration allows a considerable reduction in processing time as compared to fully sampled integration. In our work, we used random sampling over a uniform grid to compute the posterior PDF of f_s, that is, MWF. Careful selection of M, the number of sampled points used in the BMC integration, was required, given the expected slow rate of convergence of only $\sqrt{M}$ (41-42); we found that $M \simeq 20{,}000$ samples led to an extremely accurate results (Fig. 2). Other strategies may be preferred to the BMC integrations performed here, in accordance with the comment of Jaynes: "Whenever there is a randomized way of doing something, there is a non-randomized way which yields better results, but requires more thinking" (55). Indeed, other sampling strategies such as stratified sampling or Markov Chain MC may prove to be more efficient for calculating the posterior PDF of f_s (or MWF) when high-dimensional marginalization is required, as is the case here.

5.3. SRC-NLLS Analysis

The SRC algorithm as applied here and in the conventional implementation of mcDESPOT is a particular implementation of NLLS. Our results indicate that SRC-NLLS provides accurate and precise estimates of f_s, that is, MWF, from high SNR datasets (Figs. 3-4 and 7-9), in agreement with previous studies (24, 26). Further, unlike BMC, in which all parameters except the one under consideration are subject to marginalization, SRC-NLLS provides a rapid estimate of all unknown parameters simultaneously with modest computational requirements. Using SRC-NLLS, the mean ± SD of estimated values of $T_{2,s}$, $T_{2,l}$, $T_{1,s}$ and $T_{1,l}$ obtained from SNR_{High} protocol data were 17 ± 10 ms, 81 ± 13 ms, 641 ± 53 ms, and 2127 ± 229 ms, respectively. Those values are in good agreement with values reported in the literature (46, 56). However, as has been previously pointed out (46), some of those parameters may exhibit unreasonable values in certain circumstances, such as upon the incorporation of chemical exchange into the formalism. This further highlights the potential for BMC-mcDESPOT to improve upon existing higher-dimensional analyses.

Furthermore, as with any least squares-based algorithm, the accuracy of the SRC-NNLS algorithm is limited by the presence of local minima and flat LSR energy surfaces (24); this

greatly reduces the quality of parameter estimates at low-to-moderate SNR (Figs. 3-5 and 7-9). These considerations may represent an important limitation in the application of SRC-NLLS to mcDESPOT parameter estimates in the setting of modest SNR, including high-resolution whole-brain studies and studies limited by patient compliance.

5.4. mcDESPOT Analysis

We analyzed the mcDESPOT signal model without exchange for two reasons. First and foremost, the most basic form of mcDESPOT still requires a fit of five unknown parameters using SRC-NLLS or, with Bayesian analysis, marginalization over four nuisance parameters. Further, a recent study showed that the incorporation of two-site exchange has a minimal effect on estimated MWF values (46), which is the main parameter of interest. However, the extension of the BMC to incorporate exchange is straightforward. In addition, to correspond to the conventional analysis of mcDESPOT, we neglected the effects of MT between free water protons and macromolecules, inherent to all steady-state measurements on biological systems (57). However, in a recent study, Liu *et al.* (50) developed a new method termed mcRISE to account for MT effects through incorporation of a macromolecular proton pool in exchange with mcDESPOT water pools. It has been shown that MT effects have notable impact on derived short fraction estimate in human knee cartilage corresponding, presumably, to proteoglycan water fraction. On the other hand, Zhang *et al.* (56) compared mcDESPOT measurements obtained using long or short RF pulses, which result in differing amounts of MT. The results indicated that the extracted MWF values are relatively insensitive to changes in MT. Further work, including the application of the mcRISE approach to brain analysis, is required to further understand the impact of MT on MWF.

Of note is the fact that a recent *in-vivo* study indicated that MWF values derived from mcDESPOT were substantially greater than those derived from a CPMG analysis (46). This was attributed to fact that mcDESPOT and CPMG are influenced to substantially different degrees by the experimental and physiological effects that cause received signals to deviate from ideal models (24, 46). These effects include diffusion, exchange, off-resonance effects, magnetization transfer, *J*-coupling, spin locking, internal gradients, magnetization spoiling and noise. The importance of these effects in a particular experiment will depend upon both the specifics of the sample or subject under investigation and the details of the pulse sequence, including the selection of parameters such as TE, TR, FAs, and gradient durations and amplitudes. Given the substantial differences between conventional SRC-NLLS and BMC analysis of mcDESPOT, and what we believe to be the substantially improved accuracy of the latter, it is not unexpected that our results for MWF would differ from published values. Indeed, the derived MWF estimates using BMC2 and BMC3 were somewhat slightly lower than those derived using SRC-NLLS. Nevertheless, our *in-vivo* results were, overall, consistent with values reported in the literature (18-21, 32, 46, 56).

6. CONCLUSIONS

Estimation of MWF in the human brain from mcDESPOT was markedly improved through use of Bayesian analysis, especially at low-to-moderate SNR. We found that Bayesian approaches that incorporated marginalization over noise, designated BMC2 and BMC3,

demonstrated superior accuracy and precision in parameter estimation as compared to SRC-NLLS or a Bayesian method, BMC1, that incorporates naive estimation of noise assuming spatially-invariant noise. These results will be of significance for high resolution whole-brain MWF mapping. Further, BMC-mcDESPOT can readily be extended to incorporate exchange between pools and to other tissues, including, for example, the estimation of the proteoglycan-associated water fraction in cartilage (58-59).

8. ACKNOWLEDGEMENTS

This work was supported by the Intramural Research Program of the NIH, National Institute on Aging. We thank David A. Reiter, Donnie Cameron and Christopher Bergeron for their assistance with data acquisition.

7. APPENDIX

Given an i.i.d sequence of measurements {**S**} of normal random variables having mean μ and standard deviation σ, the Gaussian likelihood function, $L(\mathbf{S} \mid \mu, \sigma)$, of {**S**} is given by

$$L\left(\mathbf{S}|\mu,\sigma\right)=\left(\frac{1}{\sigma\sqrt{2\pi}}\right)^{R}\quad exp\left(-\frac{\sum_{r=1}^{R}\left(S^{r}-\mu\right)^{2}}{2\sigma^{2}}\right)$$

where R is the total length of the sequence of measurements. Assuming a Jeffreys prior on σ, that is, $P(\sigma) \propto 1/\sigma$, the marginalized likelihood function over σ is given by

$$\begin{aligned}L\left(\mathbf{S}|\mu\right)\quad&=\int_{0}^{\infty}\mathrm{P}\left(\sigma\right)l\left(\mathbf{S}|\mu,\sigma\right)\mathrm{d}\sigma=\int_{0}^{\infty}\frac{1}{\sigma}\left(\frac{1}{\sigma\sqrt{2\pi}}\right)^{R}\quad exp\left(-\frac{\sum_{r=1}^{R}\left(S^{r}-\mu\right)^{2}}{2\sigma^{2}}\right)\mathrm{d}\sigma\\&=\left(2\pi\right)^{\frac{R}{2}}\int_{0}^{\infty}\sigma^{-(R+1)}\quad exp\left(-\frac{\sum_{r=1}^{R}\left(S^{r}-\mu\right)^{2}}{2\sigma^{2}}\right)\mathrm{d}\sigma\end{aligned}\qquad [A.1]$$

Using the following change of variables: $b=\sum_{r=1}^{R}(S^{r}-\mu)^{2}$ and y = σ^2 , Equation A.1 becomes

$$\begin{aligned}L\left(\mathbf{S}|\mu\right)\quad&=(2\pi)^{\frac{R}{2}}\int_{0}^{\infty}y^{-\frac{(R+1)}{2}}\quad exp\left(-\frac{b}{2y}\right)\frac{1}{2}y^{-\frac{1}{2}}\mathrm{dy}\\&=\frac{1}{2}(2\pi)^{\frac{R}{2}}\int_{0}^{\infty}y^{-\frac{a}{2}}\quad exp\left(-\frac{b}{2y}\right)\mathrm{dy}\end{aligned}\qquad [A.2]$$

where $a\,(R+2)$.

Finally, using $\int_{0}^{\infty}\mathrm{y}^{-a/2}exp\left(-\frac{b}{2y}\right)\quad\mathrm{dy}\quad=\Gamma\left(\frac{a-2}{2}\right)\left(\frac{2}{b}\right)^{(a-2)/2}$, where and Γ is the gamma function, the marginalized likelihood function given by Equation A.2 becomes

$$L\left(\mathbf{S}|\mu\right)=\frac{1}{2}(2\pi)^{-\frac{R}{2}}\Gamma\left(\frac{a-2}{2}\right)\left(\frac{2}{b}\right)^{(a-2)/2}=\frac{\Gamma\left(R/2\right)}{2\sqrt{\pi^{R}}}\left(\sum_{r=1}^{R}\left(S^{r}-\mu\right)^{2}\right)^{-\frac{R}{2}}\qquad [A.3]$$

which is independent of σ.

REFERENCES

1. Whitaker K, Kolind S, MacKay A, Clark C. Quantifying development: investigating highly myelinated voxels in preadolescent corpus callosum. Neuroimage. 2008; 43:731–735. [PubMed: 18718540]
2. Laule C, Vavasour IM, Moore GRW, Oger J, Li DKB, Paty DW, MacKay AL. Water content and myelin water fraction in multiple sclerosis. A T2 relaxation study. Journal of neurology. 2004; 251:284–293. [PubMed: 15015007]
3. Neema M, Goldberg-Zimring D, Guss ZD, Healy BC, Guttmann CRG, Houtchens MK, Weiner HL, Horsfield MA, Hackney DB, Alsop DC, Bakshi R. 3 T MRI relaxometry detects T2 prolongation in the cerebral normal appearing white matter in multiple sclerosis. NeuroImage. 2009; 46:633–641. [PubMed: 19281850]
4. Sirrs S, Laule C, Madler B, Brief E, Tahir S, Bishop C, MacKay A. Normal appearing white matter in patients with phenylketonuria: water content, myelin water fraction, and metabolite concentrations. Radiology. 2007; 242:236–243. [PubMed: 17185670]
5. Vermathen P, Robert-Tissot L, Pietz J, Lutz T, Boesch C, Kreis R. Characterization of white matter alterations in phenylketonuria by magnetic resonance relaxometry and diffusion tensor imaging. Magn Reson Med. 2007; 58:1145–1156. [PubMed: 18046700]
6. Flynn S, Lang D, Mackay A, Goghari V, Vavasour I, Whittall K, Smith G, Arango V, Mann J, Dwork A. Abnormalities of myelination in schizophrenia detected *in-vivo* with MRI, and postmortem with analysis of oligodendrocyte proteins. Mol Psychiatr. 2003; 8:811–820.
7. Jackson GD, Connelly A, Duncan JS, Grunewald RA, Gadian DG. Detection of hippocampal pathology in intractable partial epilepsy: increased sensitivity with quantitative magnetic resonance T2 relaxometry. Neurology. 1993; 43:1793–1799. [PubMed: 8414034]
8. Wood SJ, Cocchi L, Proffitt TM, McConchie M, Jackson GD, Takahashia T, Pantelisa C, McGorryb PD, Bergerb GE. Neuroprotective effects of ethyl-eicosapentaenoic acid in first episode psychosis: a longitudinal T2 relaxometry pilot study. Psychiatry Research. 2010; 182:180–182. [PubMed: 20413278]
9. Bartzokis G, Lu PH, Mintz J. Quantifying age-related myelin breakdown with MRI: novel therapeutic targets for preventing cognitive decline and Alzheimer's disease. J Alzheimers Dis. 2004; 6:S53–9. [PubMed: 15665415]
10. Alonso-Ortiz E, Levesque IR, Pike GB. MRI-based myelin water imaging: A technical review. Magn Reson Med. 2015; 73:70–81. [PubMed: 24604728]
11. MacKay A, Whittall K, Adler J, Li D, Paty D, Graeb D. In-vivo visualization of myelin water in brain by magnetic resonance. Magn Reson Med. 1994; 31:673–677. [PubMed: 8057820]
12. Laule C, Kozlowski P, Leung E, Li DK, Mackay AL, Moore GR. Myelin water imaging of multiple sclerosis at 7 T: correlations with histopathology. Neuroimage. 2008; 40:1575–1580. [PubMed: 18321730]
13. Stewart WA, MacKay AL, Whittall KP, Moore GR, Paty DW. Spin-spin relaxation in experimental allergic encephalomyelitis. Analysis of CPMG data using a non-linear least squares method and linear inverse theory. Magn Reson Med. 1993; 29:767–775. [PubMed: 8350719]
14. Laule C, Leung E, Lis DK, Traboulsee AL, Paty DW, MacKay AL, Moore GR. Myelin water imaging in multiple sclerosis: quantitative correlations with histopathology. Mult Scler. 2006; 12:747–753. [PubMed: 17263002]
15. Whittall KP, Mackay AL, Graeb DA, Nugent RA, Li DK, Paty DW. In-vivo measurement of T2 distributions and water contents in normal human brain. Magn Reson Med. 1997; 37:34–43. [PubMed: 8978630]
16. Levesque IR, Chia CL, Pike GB. Reproducibility of in-vivo magnetic resonance imaging-based measurement of myelin water. J Magn Reson Imaging. 2010; 32:60–68. [PubMed: 20578011]
17. Prasloski T, Rauscher A, Mackay AL, Hodgson M, Vavasour IM, Laule C, Madler B. Rapid whole cerebrum myelin water imaging using a 3D GRASE sequence. Neuroimage. 2012; 63:533–539. [PubMed: 22776448]

18. Deoni SCL, Rutt BK, Arun T, Pierpaoli C, Jones DK. Gleaning multicomponent T1 and T2 information from steady-state imaging data. Magn Reson Med. 2008; 60:1372–1387. [PubMed: 19025904]
19. Deoni SCL, Dean DC, O'Muircheartaigh J, Dirks H, Jerskey BA. Investigating white matter development in infancy and early childhood using myelin water faction and relaxation time mapping. Neuroimage. 2012; 63:1038–1053. [PubMed: 22884937]
20. Dean DC, O'Muircheartaigh J, Dirks H, Waskiewicz N, Lehman K, Walker L, Piryatinsky I, Deoni SCL. Estimating the age of healthy infants from quantitative myelin water fraction maps. Hum Brain Mapp. 2015; 36:1233–1244. [PubMed: 25640476]
21. Deoni SCL, Dean DC, Remer J, Dirks H, O'Muircheartaigh J. Cortical maturation and myelination in healthy toddlers and young children. Neuroimage. 2015; 115:147–161. [PubMed: 25944614]
22. Kolind S, Matthews L, Johansen-Berg H, Leite MI, Williams SC, Deoni SCL, Palace J. Myelin water imaging reflects clinical variability inmultiple sclerosis. Neuroimage. 2012; 60:263–270. [PubMed: 22155325]
23. Kitzler HH, Su J, Zeineh M, Harper-Little C, Leung A, Kremenchutzky M, Deoni SCL, Rutt BK. Deficient MWF mapping inmultiple sclerosis using 3D whole-brain multi-component relaxationMRI. Neuroimage. 2012; 59:2670–2677. [PubMed: 21920444]
24. Bouhrara M, Reiter DA, Celik H, Fishbein KW, Kijowski R, Spencer RG. Analysis of mcDESPOT- and CPMG-derived parameter estimates for two-component non-exchanging systems. Magn Reson Med. (DOI 10.1002/mrm.25801).
25. Berger MF, Silverman HF. Microphone array optimization by stochastic region contraction. IEEE Trans Signal Process. 1991; 39:2377–2386.
26. Deoni SCL, Kolind SH. Investigating the stability of mcDESPOT myelin water fraction values derived using a stochastic region contraction approach. Magn Reson Med. 2015; 73:161–169. [PubMed: 24464472]
27. Neil JJ, Bretthorst GL. On the use of Bayesian probability theory for analysis of exponential decay data: an example taken from intravoxel incoherent motion experiments. Magn Reson Med. 1993; 29:642–647. [PubMed: 8505900]
28. Bretthorst GL, Hutton WC, Garbow JR, Ackerman JJH. Exponential Parameter Estimation (in NMR) Using Bayesian Probability Theory. Concepts in Magn Reson. 2005; 27A:55–63.
29. Kumar D, Nguyen TD, Gauthier SA, Raj A. Bayesian algorithm using spatial priors for multiexponential T2 relaxometry from multiecho spin echo MRI. Magn Reson Med. 2012; 68:1536–1543. [PubMed: 22266707]
30. Orton MR, Collins DJ, Koh DM, Leach MO. Improved intravoxel incoherent motion analysis of diffusion weighted imaging by data driven bayesian modeling. Magn Reson Med. 2014; 71:411–420. [PubMed: 23408505]
31. Bouhrara M, Reiter DA, Spencer RG. Bayesian analysis of transverse signal decay with application to human brain. Magn Reson Med. 2015; 74:785–802. [PubMed: 25242062]
32. Deoni SCL. Correction of main and transmit magnetic field (B0 and B1) inhomogeneity effects in multicomponent-driven equilibrium single-pulse observation of T1 and T2. Magn Reson Med. 2011; 65:1021–1035. [PubMed: 21413066]
33. Deoni SCL, Rutt BK, Jones DK. Investigating the effect of exchange and multicomponent T1 relaxation on the short repetition time spoiled steady-state signal and the DESPOT1 T1 quantification method. J Magn Reson Imaging. 2007; 25:570–578. [PubMed: 17326090]
34. Deoni SCL, Rutt BK, Jones DK. Investigating exchange and multicomponent relaxation in fully-balanced steady-state free precession imaging. J Magn Reson Imaging. 2008; 27:1421–1429. [PubMed: 18504765]
35. Cunningham CH, Pauly JM, Nayak KS. Saturated double angle method for rapid B_1^+ mapping. Magn Reson Med. 2006; 55:1326–1333. [PubMed: 16683260]
36. Deoni SCL. Transverse relaxation time (T2) mapping in the brain with off-resonance correction using phase-cycled steady-state free precession imaging. J Magn Reson Imaging. 2009; 30:411–417. [PubMed: 19629970]
37. Silvia, DS. Data Analysis: A Bayesian tutorial. Oxford University Press; Oxford: 1996.

38. Sijbers J, den Dekker AJ. Maximum likelihood estimation of signal amplitude and noise variance from MR data. Magn Reson Med. 2004; 51:586–594. [PubMed: 15004801]
39. Jeffreys H. An invariant form for the prior probability in estimation problems. Proc R Soc A. 1946; 186:453–461.
40. Zellner A. On assessing prior distributions and Bayesian regression analysis with g-prior distributions. Bayesian inference and decision techniques essays in honor of Bruno de Finetti. 1986; 6:233–243.
41. Barber, D. Bayesian reasoning and machine learning. Cambridge University Press; Cambridge, UK: 2012.
42. Caflisch RE. Monte Carlo and quasi-Monte Carlo methods. Acta Numer. 1998; 7:1–49.
43. Bouhrara M, Reiter DA, Celik H, Bonny JM, Lukas V, Fishbein KW, Spencer RG. Incorporation of Rician noise in the analysis of biexponential transverse relaxation in cartilage using a multiple gradient echo sequence at 3 and 7 Tesla. Magn Reson Med. 2015; 73:352–366. [PubMed: 24677270]
44. Constantinides CD, Atalar E, McVeigh ER. Signal-to-noise measurements in magnitude images from NMR phased arrays. Magn Reson Med. 1997; 38:852–857. [PubMed: 9358462]
45. Aja-Fernández S, Brion V, Tristán-Vega A. Effective noise estimation and filtering from correlated multiple-coil MR data. Magn Reson Imaging. 2013; 31:272–285. [PubMed: 23122024]
46. Zhang J, Kolind SH, Laule C, MacKay AL. Comparison of myelin water fraction from multiecho T2 decay curve and steady-state methods. Magn Reson Med. 2015; 73:223–232. [PubMed: 24515972]
47. Du YP, Chu R, Hwang D, Brown MS, Kleinschmidt-DeMasters BK, Singel D, Simon JH. Fast multislice mapping of the myelin water fraction using multicompartment analysis of T2* decay at 3T: a preliminary postmortem study. Magn Reson Med. 2007; 58:865–870. [PubMed: 17969125]
48. Lenz C, Klarhöfer M, Scheffler K. Feasibility of in vivo myelin water imaging using 3D multigradient-echo pulse sequences. Magn Reson Med. 2012; 68:523–528. [PubMed: 22213038]
49. Hwang D, Kim DH, Du YP. In vivo multi-slice mapping of myelin water content using T2* decay. Neuroimage. 2010; 52:198–204. [PubMed: 20398770]
50. Liu F, Block WF, Kijowski R, Samsonov A. Rapid multicomponent relaxometry in steady state with correction of magnetization transfer effects. Magn Reson Med. 2015 (DOI: 10.1002/mrm.25672).
51. Bouhrara M, Spencer RG. Incorporation of nonzero echo times in the SPGR and bSSFP signal models used in mcDESPOT. Magn Reson Med. 2015 (DOI: 10.1002/mrm.25984).
52. Aja-Fernández S, Alberola-López C, Westin CF. Noise and signal estimation in magnitude MRI and Rician distributed images: A LMMSE approach. IEEE Trans Image Process. 2008; 17:1383–1898. [PubMed: 18632347]
53. Aja-Fernández S, Pieciak T, Vegas-Sánchez-Ferrero G. Spatially variant noise estimation in MRI: a homomorphic approach. Med Image Anal. 2015; 20:184–197. [PubMed: 25499191]
54. Gudbjartsson H, Patz S. The Rician distribution of noisy MRI data. Magn Reson Med. 1995; 34:910–914. [PubMed: 8598820]
55. Jaynes, ET. Fragmentary Edition of March 1996, full edition in preparation. Cambridge Univ. Press; MA, USA: Probability theory: the logic of science.
56. Zhang J, Kolind SH, Laule C, MacKay AL. How does magnetization transfer influence mcDESPOT results? Magn Reson Med. (DOI: 10.1002/mrm.25520).
57. Henkelman RM, Stanisz GJ, Graham SJ. Magnetization transfer in MRI: a review. NMR Biomed. 2001; 14:57–64. [PubMed: 11320533]
58. Liu, F.; Choi, K.; Samsonov, A.; Spencer, RG.; Wilson, JJ.; Block, WF.; Kijowski, R. In-vivo multicomponent T2 relaxation time analysis of the articular cartilage of the human knee joint at 3.0T. In Press; Radiology: 2015.
59. Liu F, Chaudhary R, Hurley SA, Munoz Del Rio A, Alexander AL, Samsonov A, Block WF, Kijowski R. Rapid multicomponent T2 analysis of the articular cartilage of the human knee joint at 3.0 T. J Magn Reson Imaging. 2014; 39:1191–1197. [PubMed: 24115518]

Highlights

- We propose a significantly improved technique for estimating myelin water fraction in human brain using magnetic resonance imaging
- The proposed procedure is based on Bayesian analysis of the mcDESPOT signal model
- Detailed simulations and *in-vivo* studies indicate the superiority of this Bayesian approach as compared to conventional approach based on least-squares estimates
- These results will substantially improve the quality of high-resolution whole-brain mapping of myelination in human brain

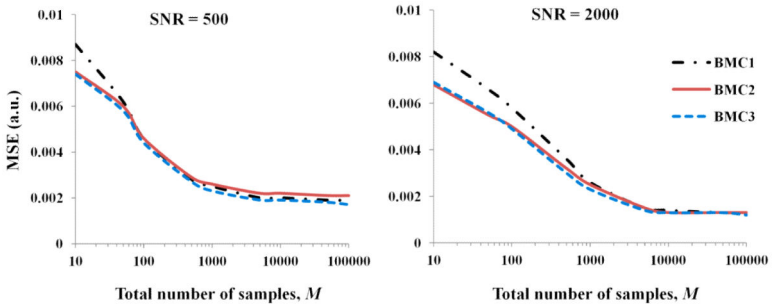

Figure 1.

MSE (Eq. 9) in the estimation of the short fraction, f_s, as a function of the total number of random samples, M, used in the BMC integration. Results are presented for two different SNR values, 500 and 2000, using the three different BMC approaches described in the text (cf. "Bayesian Analysis of mcDESPOT" section). The other underlying input parameters were fixed to values of $T_{2,s}$ = 15 ms, $T_{2,l}$ = 100 ms, $T_{1,s}$ = 450 ms and $T_{1,l}$ = 1800 ms.

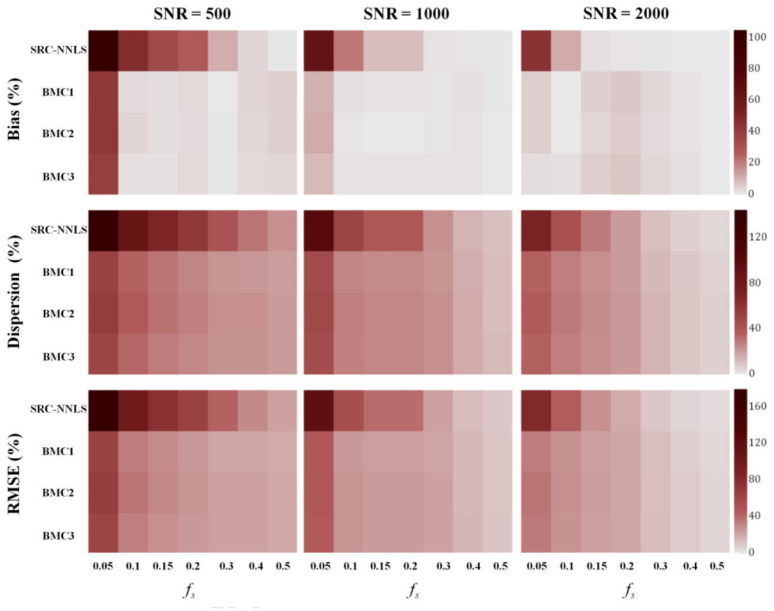

Figure 2.

Mean and standard deviation (top row), and MRE (bottom row) of f_s estimated over 1001 noise realizations obtained using fully sampled (Eq. 5) and BMC (Eq. 8) integrations for different SNR and f_s values. The other underlying input parameters were fixed to values of $T_{2,s}$ = 15 ms, $T_{2,l}$ = 100 ms, $T_{1,s}$ = 450 ms and $T_{1,l}$ = 1800 ms.

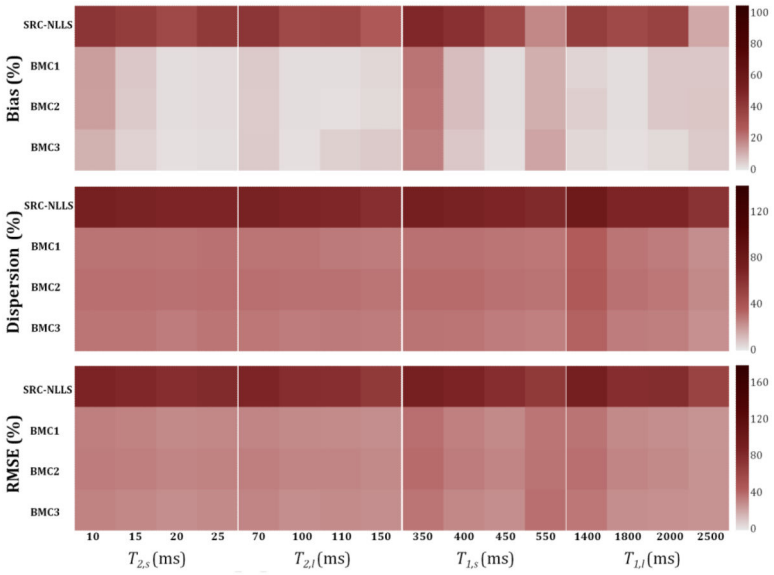

Figure 3.

Relative bias, dispersion and RMSE in the estimation of f_s using the SRC-NLLS algorithm and the three BMC approaches. Results are presented for several combinations of SNR and f_s values. The other underlying input parameters were fixed to values of $T_{2,s}$ = 15 ms, $T_{2,l}$ = 100 ms, $T_{1,s}$ = 450 ms and $T_{1,l}$ = 1800 ms.

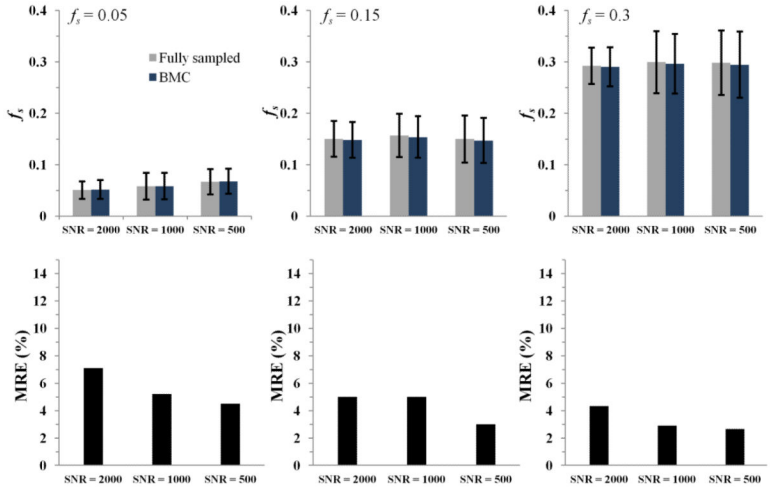

Figure 4.

Relative bias, dispersion and RMSE in the estimation of f_s using the SRC-NLLS algorithm and the three BMC approaches. Results were obtained by fixing the f_s and SNR values to 0.15 and 500, respectively, and varying the values of the remaining parameters. Values used were $T_{2,s}$ = (10, 15, 20, 25) ms, $T_{2,l}$ = (70, 100, 110, 150) ms, $T_{1,s}$ = (350, 400, 450, 550) ms and $T_{1,l}$ = (1400, 1800, 2000, 2500) ms.

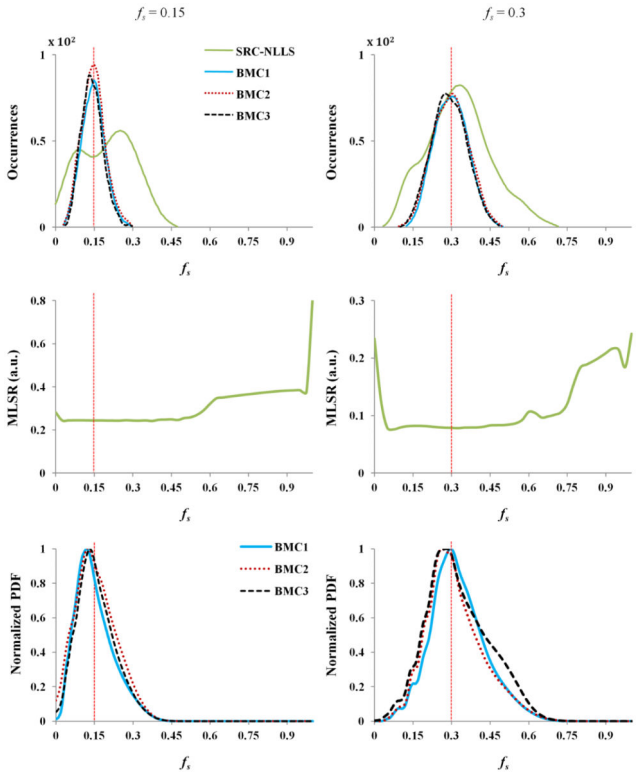

Figure 5.

Top row: The histogram of f_s estimates obtained from 1001 noise realizations using the SRC-NLLS algorithm and BMC. Middle row: Minimum least squares residual (MLSR) of f_s as a function of f_s for a single noise realization. Bottom row: The normalized posterior probability density function (PDF) of f_s as a function of f_s obtained using BMC for a single noise realization. Normalization was performed with respect to the maximum value of each corresponding posterior PDF. In each case, the vertical red line indicates the true input value of f_s. Results are presented for data generated with SNR of 500 and for two true input f_s values of 0.15 (left column) and 0.3 (right column). The other underlying input parameters were fixed to $T_{2,s}$ = 15 ms, $T_{2,l}$ = 100 ms, $T_{1,s}$ = 450 ms and $T_{1,l}$ = 1800 ms.

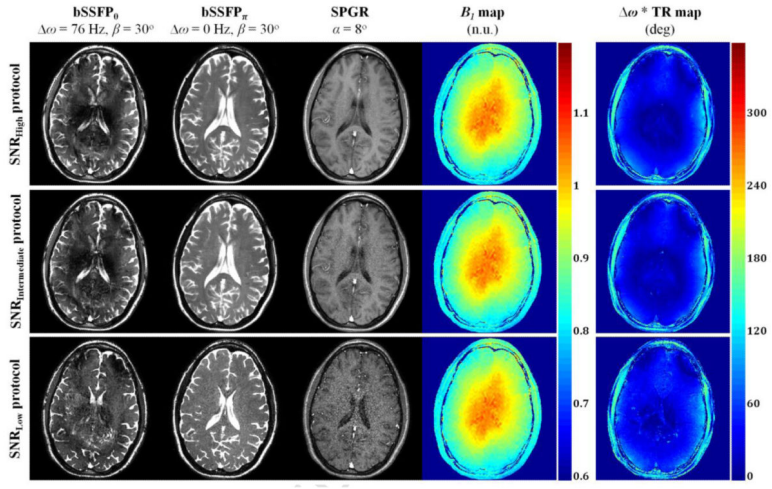

Figure 6.

Representative examples of axial bSSFP and SPGR weighted-images and the corresponding B_1 and $\Delta\omega$ * TR maps calculated using S-DAM and DESPOT2-FM, respectively. Results are presented for each of the three protocols described in the text (see "Materials and Methods"). SNR_{High} ($\simeq 90$) represents the highest SNR datasets, $SNR_{Intermediate}$ ($\simeq 40$) represents the intermediate SNR datasets, and SNR_{Low} ($\simeq 25$) represents the lowest SNR datasets.

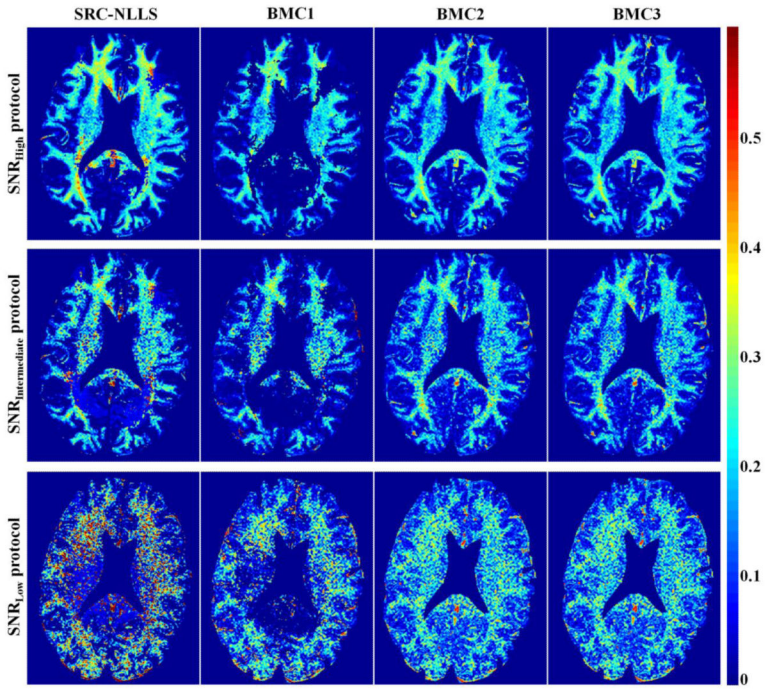

Figure 7.

Representative f_s maps, reflecting the spatial distribution of MWF, derived from in-vivo brain images using the SRC-NLLS algorithm and the three BMC approaches described in the text. MWF maps were derived from the SNR_{High} ($\simeq 90$), $SNR_{Intermediate}$ ($\simeq 40$) and SNR_{Low} ($\simeq 25$) datasets as described in the text.

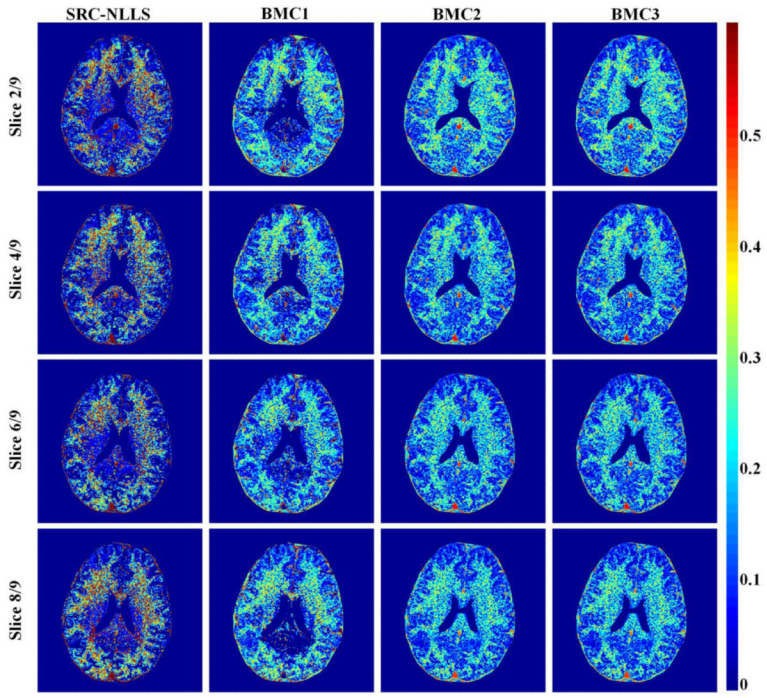

Figure 8.

MWF maps derived from in-vivo brain images using the SRC-NLLS algorithm and the three BMC approaches described in the text. MWF maps were derived for different slices from the SNR_{Low} ($\simeq$ 25) datasets.

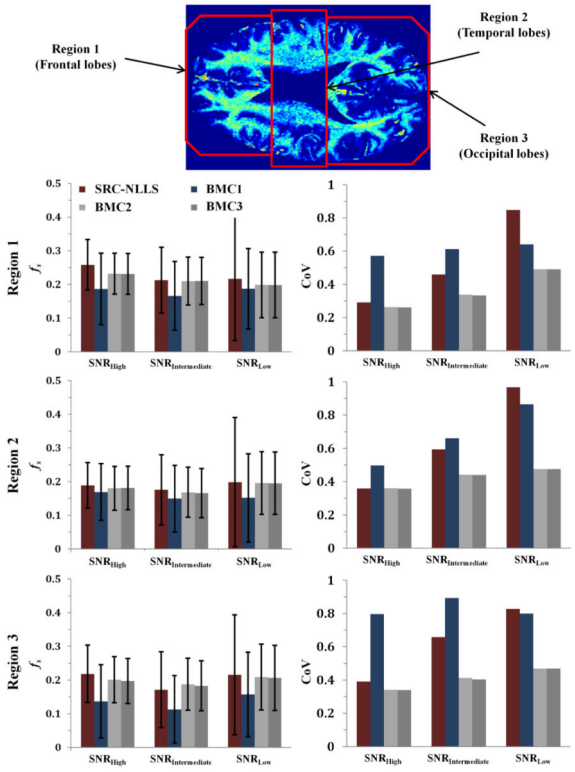

Figure 9.

Left column: means and standard deviations of estimates of f_s, reflecting MWF, calculated in the three brain regions indicated in the above illustration from the SNR_{High} ($\simeq 90$), $SNR_{Intermediate}$ ($\simeq 40$),and SNR_{Low} ($\simeq 25$) protocols. In each case, results obtained from SRC-NLLS and the three BMC approaches described in the text are presented. Right column: the corresponding coefficients of variation (CoV).

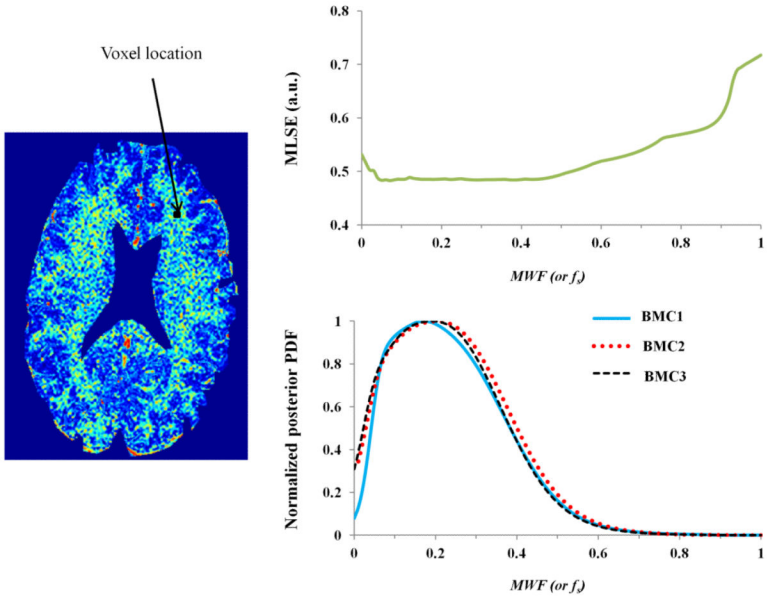

Figure 10.

Minimum least squares residual (MLSR) of f_s, representing MWF, as a function of f_s, and the normalized posterior probability density function (PDF) of f_s as a function of f_s obtained using the three BMC methods. Results were obtained from a single voxel from datasets obtained with SNR_{Low} ($\simeq$ 25). Normalization was performed with respect to the maximum value for each posterior PDF.

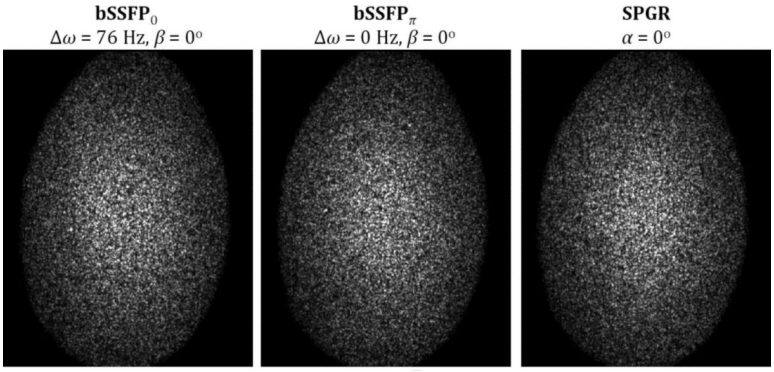

Figure 11.

Examples of magnitude noise images obtained using the SPGR and bSSFP sequences with null FA. As can clearly be seen, noise exhibited substantial spatial variation.

Table 1

Effect of error in σ on the degree of bias, calculated as ΔBias = |Bias (exact σ) - Bias (estimated σ)| and on the degree of variation, calculated as ΔDispersion = |Dispersion (exact σ) - Dispersion (estimated σ)| in estimated f_s using the BMC 1 approach. Results were obtained from 1001 noise realizations for three representative SNRs and for assumed errors in the estimation of σ of 10% and 20% and 50%. The underlying input parameters were fixed at $f_s = 0.15$, $T_{2,s} = 15$ ms, $T_{2,l} = 100$ ms, $T_{1,s} = 450$ ms and $T_{1,l} = 1800$ ms. As indicated, ΔBias and ΔDispersion were negligible for moderate errors (≤ 20%) in σ.

Error (%)	**10**			**20**			**50**		
SNR	500	1000	2000	500	1000	2000	500	1000	2000
ΔBias (%)	4	0	0	5	1	1	7	4	3
ΔDispersion (%)	3	2	1	6	4	2	10	8	5